Superelastic electron collisions with silver: Measuring the angular momentum transferred to the target during the collision

Sarah Jhumka, Kate L. Nixon, Martyn Hussey, and Andrew James Murray[*]
Photon Science Institute, School of Physics and Astronomy, University of Manchester, Manchester M13 9PL, United Kingdom

Superelastic electron-collision studies have been carried out with a transition-metal target. ^{107}Ag atoms were excited from the $5\ ^2S_{1/2}(F = 1)$ ground state to the $5\ ^2P_{3/2}(F' = 2)$ excited state using continuous-wave circularly polarized laser radiation at $\sim$328.1 nm. An electron beam of well-defined energy E_{inc} then deexcited the targets, and the superelastically scattered electrons that gained energy from the collision were detected as a function of scattering angle and laser polarization. Results for the angular momentum $L_\perp$ transferred to the target are presented over a range of scattering angles, for six outgoing energies from $E_{out} = 100$ eV down to 20 eV.

　　　　　　　　　PACS number(s): 34.80.Dp

I. INTRODUCTION

Precise details of the collision between an electron and atom leading to target excitation normally require the scattered electron to be detected in time coincidence with fluorescence emitted from the target as it relaxes to a lower state [1]. The yield from these experiments is often very low due to the small collection angles of the detectors. An alternative is the superelastic scattering technique, as adopted here [2–14]. In these experiments the target is initially excited by resonant laser radiation of the same energy as the detected fluorescence photon in the coincidence experiment. An electron beam is directed at the laser-excited target with a well-defined momentum and energy E_{inc}, such that this energy is equal to that of the inelastically scattered electron in coincidence studies. Superelastically scattered electrons that have gained energy from the excited targets are then detected as a function of the scattering angle and polarization of the laser beam. This yields an equivalent set of data (known as the atomic collision parameters, or ACPs [15]) as are obtained using the coincidence technique; however, the data collection rate can be thousands of time faster.

In both types of experiment a comparison with theoretical calculations of the interaction is possible through the ACPs. These parameters were introduced to describe an electron-excited P state in the target, which is the type of state most frequently studied. The parameters include P_{lin} and γ, which describe alignment of the P state, and $L_\perp$ which measures the angular momentum transferred to the target during the collision. The direction of the angular momentum is orthogonal to the scattering plane set by the momenta of the incident and outgoing electrons. A fourth parameter ρ_{00}^A describes the probability that the electron spin changes during the collision.

In the superelastic experiments described here only $L_\perp$ was determined. Figure 1 shows the adopted geometry. A frequency-doubled continuous-wave (cw) laser beam was directed through the interaction region so that the beam was orthogonal to the scattering plane. The laser beam was circularly polarized using a linear polarizer and $\lambda/4$ plate. A

gun produced an electron beam of well-defined energy E_{inc} that was incident onto the atomic beam. Two electron analyzers were located in the scattering plane around the interaction region, so as to detect electrons scattered through angles θ_1 and θ_2 from the target atoms. The analyzers each detected electrons with energy E_{out}. Direct comparison to coincidence studies then requires $E_{out} = E_{inc}^{Coinc}$, and $E_{inc} = E_{out}^{Coinc}$. In this paper all results are quoted for values of E_{out}, ranging from 100 to 20 eV. Since the analyzers were on opposite sides of the incident electron beam, when $|\theta_1| = |\theta_2|$, $L_\perp(\theta_1) = -L_\perp(\theta_2)$. This relationship allows the data from both analyzers to be related to a common scattering angle θ_e.

One of the key motivations in carrying out these superelastic scattering experiments from silver was to determine if the presence of the d electrons in this transition-metal target play a role in determining the detailed scattering dynamics. Silver is similar to the alkali targets that have been extensively studied using the superelastic technique, since silver has a single electron in the outer valence shell (the $5s$ electron). However, unlike alkali atoms that have the preceding shell filled with p electrons, this shell in silver is filled with ten $4d$ electrons whose excitation energy is relatively low. Interactions with both $4d$ and $5s$ electrons during the electron-scattering process may then lead to significantly different collision parameters compared to alkali targets.

Previous electron-collision experiments with silver have measured elastic and inelastic cross sections from this target, although comparatively few have been performed due to the technical difficulties of producing a well-defined atomic beam of silver. Examples include the early work of Blais and Mann [16], who measured the ionization probability as a function of incident electron beam energy. Smirnov [17] used a crossed-beam technique to measure excitation cross sections for more than 200 levels of silver, at an incident electron energy of 50 eV. The group of Tošić and co-workers in Belgrade [18,19] recently measured elastic and inelastic differential cross sections from silver at incident electron energies up to 100 eV, and compared their results to relativistic distorted wave calculations carried out by Stauffer and colleagues. No previous measurements of partial differential cross sections (as represented by the ACPs) have been obtained for silver either using coincidence techniques, or using superelastic methods.

———————
[*]Email address: Andrew.Murray@manchester.ac.uk
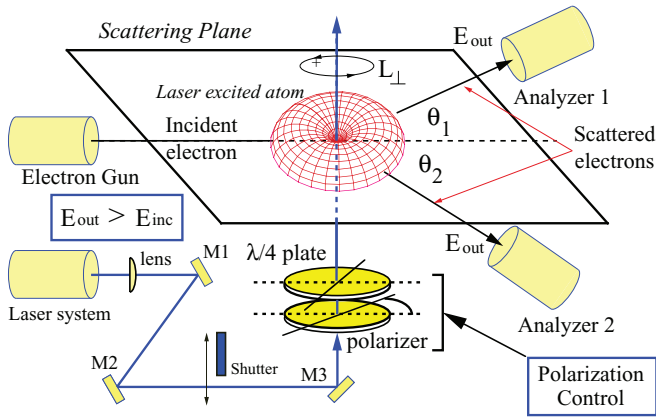
FIG. 1. (Color online) The superelastic scattering geometry adopted here. The laser beam was directed by mirrors M1–M3 so as to be incident from below the scattering plane. The laser polarization was set to produce an oriented target. Electrons from the gun that were scattered by the target atoms were detected using two electron analyzers. The scattering plane is defined by the momenta of the incident and scattered electrons. Both outgoing electrons were detected in this plane.

FIG. 2. (Color online) The experimental apparatus as viewed from above the scattering plane. The positions of the analyzers at their maximum and minimum angles are shown. For details see text.

For the present superelastic scattering experiments from silver, the excitation energy requires laser radiation at around 328.1 nm, equivalent to an excitation energy E_{exc} from the $4d^{10}5s\ ^2S_{1/2}$ ground state to the $4d^{10}5p\ ^2P_{3/2}$ state of $\sim$3.778 eV. The relationship between incident and outgoing electron energies for silver is then given by

$$E_{out} = E_{inc} + 3.778 \text{ eV}. \tag{1}$$

The incident electron beam therefore needs to be 3.778 eV *lower* in energy than the electrons selected by the analyzers.

To clarify the present work, this paper is divided into four sections. The experimental procedures used to collect the data are detailed in Sec. II, where the laser system and spectrometer are described. The measurements required data accumulation times of several weeks, and so the techniques used to ensure the apparatus was stable over this period of time are discussed. Section III shows the experimental data for $L_\perp$, taken over a range of scattering angles from $\theta_e = 20°$ to $\theta_e = 130°$. Six energies were selected for these measurements, so that the evolution of $L_\perp$ could be seen as a function of both scattering angle and energy. Conclusions and future work are then outlined in Sec. IV.

II. EXPERIMENTAL PROCEDURES

Figure 2 is a schematic of the electron spectrometer as viewed from above the scattering plane. The silver atomic beam was produced from a custom-built oven that used six heaters. Each heater was constructed from a 300-mm length of 0.125-mm-diameter tungsten wire wound around a pure Al_2O_3 thin-walled tube of length 98 mm [20]. The wire was wound as a double spiral around the ceramic tube, so that magnetic **B** fields generated by current passing through the wire are minimized. The drive current to the heaters was supplied by six high-power sound-reinforcement amplifiers
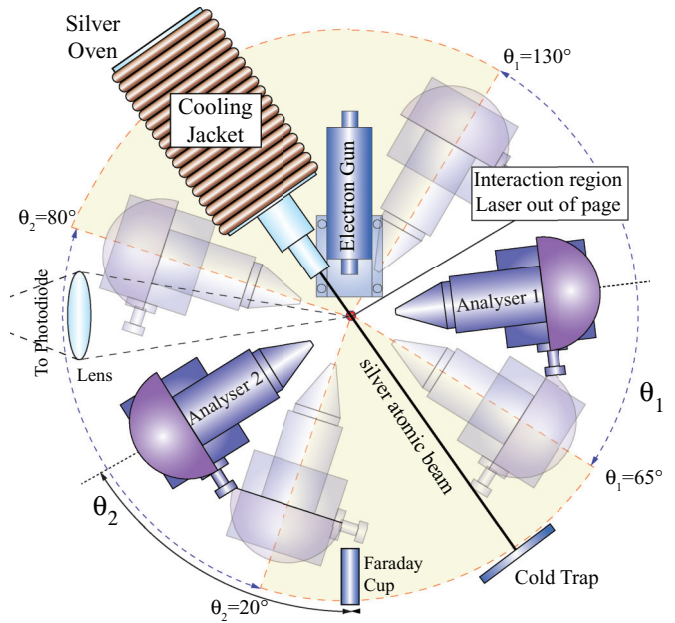
operating at 10 kHz [21]. This arrangement was chosen as it allows the sinusoidal drive current to be switched off at the zero crossing point of the ac signal, allowing complete elimination of any **B** fields produced by the heater current. For the present experiments this was found not to be necessary, as the field generated by the heaters at the interaction region was measured to be less than 3 mG.

To produce an atomic beam of sufficient density the oven had to operate at a temperature of $\sim$1450 K, and so specialized materials were needed for construction of both the furnace and crucible in the oven. The furnace was constructed of boron nitride surrounded by six molybdenum heat shields. The crucible was constructed from graphite. A 1-mm-diameter 10-mm-long nozzle was drilled into the graphite crucible so as to quasicollimate the silver beam effusing from the nozzle. The temperature of the furnace was monitored using a tungsten-rhenium thermocouple [22]. Additional heat shields were placed both in front of and behind the furnace, so as to reduce the heat flux into the vacuum system, and also reduce the input power requirements. An oxygen-free copper cylindrical jacket surrounded the heat shields, this jacket being cooled by passing water through copper pipes wound tightly around and connected to the jacket. Cold water was passed through flexible stainless tubing connected to these copper pipes using Swagelok fittings.

Further collimation of the atomic beam was carried out using a skimmer and aperture assembly located on the front of the oven. The final output aperture of this assembly was 2 mm in diameter placed 62 mm in front of the oven nozzle, so that the angular spread of the resulting atomic beam was $\pm$1.5°. This was confirmed by measuring the diameter of the silver spot that deposited onto the liquid nitrogen cooled cold trap located 210 mm beyond the interaction region. The size of the atomic beam at the interaction region was then determined to

be ∼3 mm in diameter. The temperature of the oven as used in these studies corresponds to a Doppler width of ∼42 MHz [8].

The electron beam was produced by a two-stage electron gun, using a design that has been detailed in previous publications [23]. The gun can deliver a collimated electron beam with a current of up to 5 μA at the interaction region for an incident energy around 100 eV, as measured in a Faraday cup. The electron beam current reduced to ∼300 nA at an incident electron energy of ∼16.2 eV (i.e., for $E_{out} = 20$ eV). The energy of the electron beam was calibrated against the known 19.366 eV elastic resonance in helium [24], by injecting helium gas through a capillary directed into the interaction region while the oven was operating. An offset contact potential of ∼1 eV was determined from these measurements. The pass energies of the electron analyzers were then set using inelastic scattering data from the helium target gas. These calibration runs were carried out regularly as the experiment proceeded, so as to allow for any alteration in the contact potential due to deposition of silver onto different parts of the spectrometer. Only small changes in the contact potential were observed during several months of operation, indicating that this unwanted deposition was minimized due to the high collimation of the atomic beam.

Two identical analyzers were used in the experiments, since this allows future (e,2e) measurements to also be carried out from laser-excited targets [25]. The analyzers consisted of a three-element electrostatic lens that imaged incoming electrons from the interaction region onto the entrance aperture of a hemispherical energy selector. The entrance apertures to the lenses limited the angular acceptance to ±3°. Electrons of a given energy passed around the energy selector and were detected by channel electron multipliers (CEMs). Signal pulses from the CEMs were amplified in custom-designed preamplifiers [26] before being passed to ORTEC 473A constant fraction discriminators. The discriminators produced slow NIM pulses that were counted using a Labview PCI 6221 data acquisition card. The count rates were also monitored using ORTEC 449-2 rate meters, which produced an output that was used to optimize the superelastic scattering signal.

Analyzer 1 can rotate through angles from $\theta_1 = 65°$ to $\theta_1 = 130°$, whereas analyzer 2 can rotate from $\theta_2 = 20°$ through to $\theta_2 = 80°$. The limitations at the higher scattering angles (shown as *inaccessible regions* in Fig. 2) were set by the physical size of the analyzers, electron gun, and oven. In the forward-scattering region, analyzer 1 was prevented from moving below $\theta_1 = 65°$ to ensure the atomic beam did not enter the analyzer lens. Analyzer 2 was limited to $\theta_2 \geqslant 20°$, to ensure the incident electron beam did not scatter from the side of the analyzer.

The spectrometer was located inside a 760-mm-diameter 600-mm-high vacuum chamber pumped by a 400-l/s turbo-molecular pump and 30-l/s scroll pump. The chamber was constructed entirely of 310-grade stainless steel and was lined internally with μ metal, so as to reduce the ingress of any external **B** fields to less than 5 mG at the interaction region. All internal components were manufactured from nonmagnetic 310-grade stainless steel, molybdenum, or titanium. The analyzers rotated on two concentric titanium turntables driven by stepper motors through 250:1 gearboxes. Their angles were

calibrated using an internal LED-photodiode coupler system that triggered at every 5° angle.

A 750-mm focal length lens quasicollimated the radiation from the laser system. Two UV-grade mirrors steered the light to a final mirror that redirected the radiation in a vertical direction orthogonal to the scattering plane (see Fig. 1). Laser radiation was then injected into the vacuum chamber through a high-quality fused-silica CF70 window located on the bottom flange of the vacuum chamber. The polarization of the laser was set using a BBO Glan-laser polarizer located in the beam path after the final mirror [27], followed by a zero-order $\lambda/4$ plate [28]. The optical axis of the $\lambda/4$ plate was set relative to the polarization axis, by retroreflecting the laser radiation back through the $\lambda/4$ plate and polarizer, so that the intensity of the returning radiation was minimized. A stepper motor then controlled the rotation of the $\lambda/4$ plate, so as to produce right- and left-hand circular radiation at the interaction region.

Fluorescence from laser excitation of the silver target beam was collected using a 50-mm-diameter 75-mm focal length fused-silica lens located inside the vacuum chamber, the radiation passing through a second fused-silica CF70 window at the side of the vacuum chamber. The lens imaged the fluorescence onto an external silicon carbide (SiC) quadrant photodiode, allowing excitation of the atomic beam by the laser beam to be monitored. The photodiode was insensitive to visible light, and so band-pass wavelength filters were not required. The fluorescence image could easily be seen on white paper, making initial alignment of the photodiode straightforward. The position of the photodiode was then adjusted using an *XYZ* adjuster to maximize the signal. The fluorescence was continuously monitored to ensure that the laser wavelength was set to maximize the population of excited targets in the interaction region.

The laser system was comprised of a Spectra Physics Millenia 15 W Nd:YVO$_4$ laser operating at 532 nm that pumps a Spectra Physics Matisse Dx-series dye laser. The dye laser linewidth was stabilized to ∼10 kHz using active intracavity optics and electronics. The frequency of the dye laser was monitored using a High Finesse WS-U wavemeter, which has an accuracy of 1 MHz. The wavemeter was, in turn, calibrated every 5 min to a frequency-stabilized helium neon laser, whose absolute frequency was measured to ∼100 kHz. The wavemeter then controlled the overall stability of the dye laser, to ensure the final laser frequency remained on resonance with the atomic transition over long periods of time.

The output from the dye laser passed to a Spectra Physics WaveTrain frequency doubler, which generated the final radiation at ∼328.1 nm. The efficiency of the frequency doubler was ∼16%, so that 1000 mW of radiation from the dye laser produced ∼160 mW of UV radiation from the doubler. This radiation then passed to the collimating, steering, and polarizing optics described above, before being injected into the experiment.

A critical requirement of the laser system was that it must be stable in frequency for long periods of time, and the enhancement cavity in the WaveTrain doubler must remain resonant with the fundamental radiation from the dye laser throughout data collection. The Spectra Physics laser system satisfied both of these demands, and was found to remain

on resonance with the selected atomic transition for up to 15 days of continuous operation. It was this stability that allowed the experimental data presented in this paper to be accumulated over the relatively short operating period of only four months.

III. EXPERIMENTAL DATA

Naturally occurring silver has two stable isotopes. ^{107}Ag is slightly more abundant, with 51.83% of the atoms being of this species. The remaining 48.16% occur as ^{109}Ag. Both isotopes have a nuclear spin $I = 1/2$. The ground state of silver is the $4d^{10}5s\ ^2S_{1/2}$ state, and so the hyperfine quantum numbers take values $F = 1$ and $F = 0$. The laser-excited state at ~ 328.1 nm is the $4d^{10}5p\ ^2P_{3/2}$ state, and so the possible values of hyperfine quantum number are $F' = 2$ and $F' = 1$ (primes are used here to denote the upper state). In both cases, the hyperfine states are inverted so that the state of lower energy has the higher quantum number.

A. Calibration of the laser wavelength to the silver transition

In the superelastic scattering experiments detailed here, ^{107}Ag was excited by the laser beam, with the $4d^{10}5s\ ^2S_{1/2}(F = 1)$ ground state to $4d^{10}5p\ ^2P_{3/2}(F' = 2)$ excited-state transition being chosen. Figure 3 shows the fluorescence measured by the SiC photodiode, as a function of laser frequency and input power into the vacuum system. Both ^{109}Ag and ^{107}Ag fluorescence peaks are seen, corresponding to transitions from $F = 1$ to $F' = 2$. The difference in the peak positions of 411 MHz arises due to the energy shift in the ground and excited states for each target, as depicted in the inset

figure. The excitation frequency of each peak is shown relative to a laser frequency of 913 546 000 MHz. The vacuum wavelengths of the transitions are hence 328.163 2370 nm for ^{109}Ag$(F = 1 \rightarrow F' = 2)$, and 328.163 0894 nm for ^{107}Ag $(F = 1 \rightarrow F' = 2)$.

The results in Fig. 3 show spectra for two different laser powers, corresponding to an average intensity in the interaction region of ~ 8 mW/mm^2 (105 mW input power) and ~ 1 mW/mm^2 (15 mW input power). A Voigt profile has been fitted to the data to estimate the full width at half maximum (FWHM) of the observed peaks. The natural linewidth of this transition in silver is 23 MHz. At the lower intensity of ~ 1 mW/mm^2 the linewidth has increased to ~ 56 MHz, due to a small amount of power broadening (contributing to a linewidth of ~ 33 MHz), convolved with the Doppler profile of the atomic beam. At the higher intensity (as used in the superelastic scattering studies detailed here) the total linewidth increases to ~ 80 MHz. Power broadening is the dominant mechanism at this intensity, contributing ~ 72 MHz to the linewidth.

These data show the effects of the broadening processes, which play an important role in determining the efficiency of production of excited atoms in the interaction region. Since only ^{107}Ag atoms are coupled by the laser, 48.16% of the atoms in the interaction region (i.e., the ^{109}Ag species) do not participate. By assuming the remaining atoms are optically pumped into a closed two-level system (between the $|F = 1, m_F = \pm 1\rangle$ states and $|F' = 2, m_{F'} = \pm 2\rangle$ states), an upper limit can be estimated for the total fraction of excited atoms in the interaction region. This indicates that for an input power of 105 mW and a Doppler width of 42 MHz (as used here), $\sim 33\%$ of the ^{107}Ag atoms are excited to the $F' = 2$ state. The *maximum* number of silver atoms in the interaction region that can be laser-excited to the $4d^{10}5p\ ^2P_{3/2}$ is then only $\sim 17\%$. This is an upper limit, since the frequency shift between $F' = 2$ and $F' = 1$ states is comparable to the broadened linewidth of the transitions. In this case there will also be significant excitation to the $F' = 1$ state when the laser is on resonance with the $F' = 2$ state. Atoms excited to the $F' = 1$ state may then spontaneously decay to the $F = 0$ state, after which they will no longer participate in the laser interaction. This leads to a further decrease in efficiency, with the consequence that the steady-state population fraction of excited targets will reduce to less than 17%.

It is possible to optically drive all participating atoms into a two-level system by adopting a second repump laser beam that recouples the $F = 0$ ground state to the $F' = 1$ excited state [29]; however, we did not have the facilities for this. It is also possible to use an electro-optic modulator (EOM) to add sidebands to the laser beam; however, at these UV wavelengths it is difficult to inject more than 2%–3% of the total energy into these sidebands. Fortunately the use of circular excitation (as required for measurements of $L_\perp$) results in fairly rapid optical pumping into the closed cycle between the $|F = 1, m_F = \pm 1\rangle$ and $|F' = 2, m_{F'} = \pm 2\rangle$ states. This reduces spontaneous emission losses to the $F = 0$ state, compared to experiments that use linearly polarized radiation where this is not possible [30]. It is for this reason we show results only for $L_\perp$ at the present time.
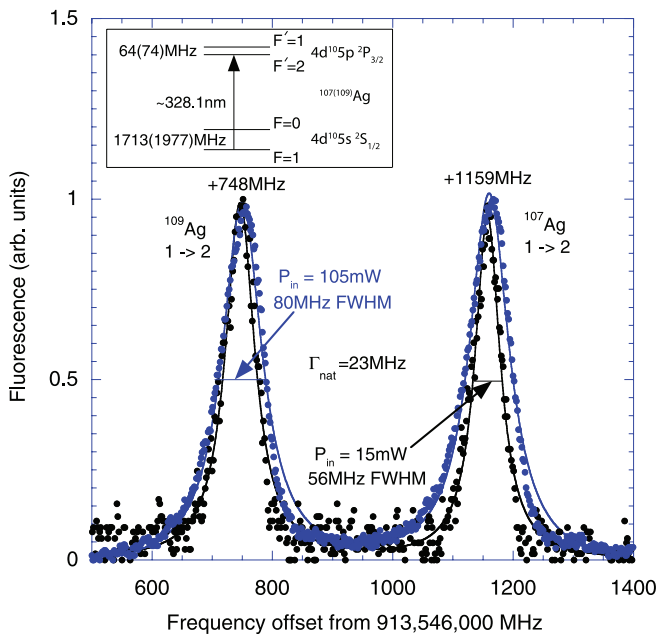
FIG. 3. (Color online) Fluorescence spectra as observed using the SiC photodiode, normalized to unity at two different input laser powers (P_{in}). The inset shows ground- and excited-state hyperfine splitting for both ^{107}Ag and ^{109}Ag (in brackets).
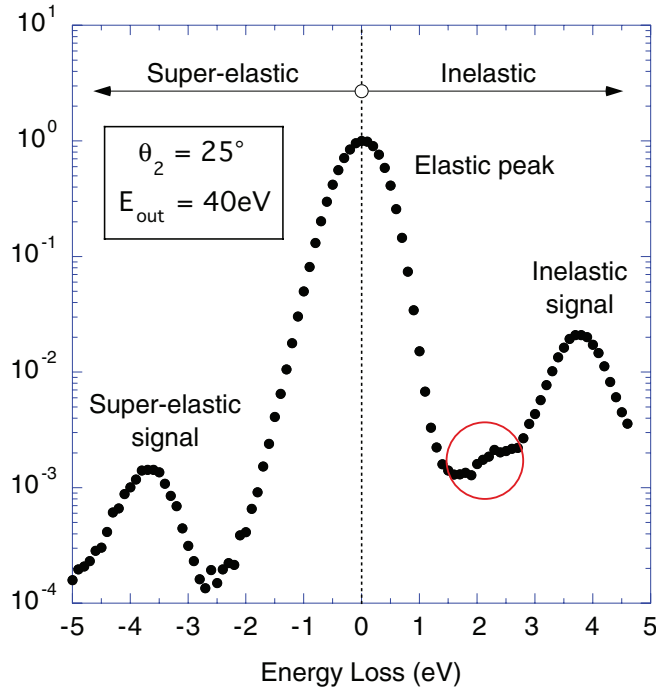
FIG. 4. (Color online) Energy loss and gain spectrum from electron interactions with Ag atoms in the interaction region, referenced to the position of the elastic peak.

B. Energy loss spectra

Figure 4 shows the electron energy loss and gain spectrum measured with analyzer 2 set to $\theta_2 = 25°$, plotted on a logarithmic scale. The outgoing electron energy used to obtain these data was 40 eV. The elastic peak dominates the spectrum, and has been set here to zero energy loss. The superelastic scattering signal located at -3.778 eV is well resolved, and has a peak intensity ~ 700 times smaller than the elastic peak. The inelastic peak located around $+3.8$ eV arises from direct electron excitation of the $4d^{10}5p\ ^2P_{3/2,\ 1/2}$ states, and is found to have a peak intensity ~ 50 times smaller than the elastic peak. The small feature (shown with a circle) arises from inelastic scattering of electrons from laser-excited atoms to higher states. Such a feature has been observed previously in ionization studies with laser-excited magnesium [25].

C. Calculation of $L_\perp$

The angular momentum parameter $L_\perp$ was determined by initially setting the $\lambda/4$ plate at an angle of $45°$ to the BBO polarizer axis (as detailed in Sec. II). The $\lambda/4$ plate was then rotated through increments of $90°$, so that pure circularly polarized radiation of opposite handedness was produced at each increment. Thirteen measurements were taken for each set of scattering angles (θ_1, θ_2) by rotating through three complete revolutions of the $\lambda/4$ plate. The superelastic signal was accumulated for up to 500 s at each angle of the retardation plate. After each measurement a shutter was inserted into the laser beam line (see Fig. 1) and a background count obtained for an equal time. The nett superelastic signal $S^n_{\sigma\pm}(\theta_e)$ was then calculated by subtracting the background count from the signal count. Six data sets were collected using σ^+

polarization, and seven were collected using σ^- polarization at each scattering angle. The results were then averaged to produce a final superelastic signal $\langle S_{\sigma\pm}(\theta_e)\rangle$. The angular momentum transferred to the atom $L_\perp$ was calculated using Eq. (2) [15]:

$$L_\perp = K^{\text{circ}} \left(\frac{\langle S_{\sigma^-}(\theta_e)\rangle - \langle S_{\sigma^+}(\theta_e)\rangle}{\langle S_{\sigma^-}(\theta_e)\rangle + \langle S_{\sigma^+}(\theta_e)\rangle} \right), \qquad (2)$$

where K^{circ} is the optical pumping parameter for circularly polarized radiation. Previous studies with other targets indicate that K^{circ} is expected to be very close to unity (typical values being ~ 0.998 [30]), so for the data presented here we have set $K^{\text{circ}} = 1$.

The sign of $L_\perp$ determined from the two analyzers was adjusted to allow for the usual convention adopted for the scattering angle in these types of experiments. For superelastic scattering, θ_e is defined as positive for scattering on the right of the incident electron beam when looking down onto the scattering plane, as noted in [15] (i.e., θ_2 is positive in the current experiments). Similarly, $L_\perp$ is positive if the angular momentum is given by the right-hand rule for the z axis in the direction of the laser beam, as shown in Fig. 1. In this case the sign of $L_\perp$ determined from analyzer 1 must be reversed, so as to meet these conventions. Direct comparison to theoretical calculations can then be made.

Figure 5 shows the results of this data analysis, for six outgoing electron energies ranging from 100 to 20 eV. The data were collected over scattering angles ranging from $\theta_e = 20°$ to $\theta_e = 130°$, taken every $2.5°$. Angular momentum conservation requires $L_\perp = 0$ at $\theta_e = 0°$ and $180°$, and these data points are also shown. $L_\perp$ is constrained to lie between ± 1 from Eq. (2), and these limits are depicted as dotted lines on the graphs.

At the highest energy of 100 eV, $L_\perp$ is seen to quickly rise from $L_\perp = 0$ at $\theta_e = 0°$ to a value ~ 0.8 at $\theta_e = 20°$, then drop to -0.1 at $\theta_e = 40°$ before once again rising to a value near 0.8 at $\theta_e = 55°$. $L_\perp$ then rapidly changes to a value of -0.93 at $\theta_e = 75°$. At higher scattering angles $L_\perp$ remains negative, slowly rising towards zero as θ_e increases. As the outgoing electron energy decreases to 50 eV, the value of $L_\perp$ in the forward-scattering region increases to close to unity, and the minima and maxima in the distribution move to higher angles. The minimum value of $L_\perp$ reduces to a value around -0.77. This trend continues as the energy reduces further to 30 eV, with the minimum between the positive peaks deepening to larger negative values. At 30 eV the forward peak evolves into two peaks, with a shallow minimum found at $\theta_e \sim 32.5°$. This minimum deepens as the energy decreases further, and the overall magnitude of the forward structure decreases. The second positive peak located at $\theta_e = 55°$ for 100 eV broadens, moves to higher angles as the energy decreases, and the magnitude of this peak diminishes. The minimum at $\theta_e \sim 75°$ for 100 eV also moves to higher angles as the energy decreases. At 30 eV this minimum is no longer distinguishable, and the value of $L_\perp$ reaches -1.0 at $\theta_e \sim 130°$.

The data at the lowest energies of 25 and 20 eV have significantly less precision at higher scattering angles, due to poor signal to noise ratio in the data at these energies. The results at 25 eV show that the maxima and minima in $L_\perp$ continue to evolve as the energy is lowered. At 20 eV the data in the forward direction clearly show the continuing evolution

FIG. 5. (Color online) Measurement of $L_\perp$ over the range of outgoing energies from 100 to 20 eV.

IV. CONCLUSIONS

Superelastic scattering data from the transition metal silver have been presented for the $L_\perp$ angular momentum parameter. These results range over energies from 100 to 20 eV, which covers the region where different models of the interaction have proven successful for alkali and alkali-earth targets. As a transition element, silver has the added complexity of ten d electrons in the outer $4d$ orbital, and these are expected to play a significant role in the scattering dynamics. Data have hence been obtained over a wide range of scattering angles from $\theta_e = 20°$ to $130°$, allowing the variation in $L_\perp$ to be characterized in detail.

The experiments proved to be difficult due to the requirement for high-intensity UV radiation, which has only recently become available using commercial sources. Further, the relative abundance of the different stable isotopes meant that only a small fraction of the atoms in the interaction region could be excited using single-mode laser radiation. Long accumulation times were hence required to ensure accurate data were obtained. This is challenging as both the electron spectrometer and laser system needed to be stable over this period of time. The methods that were used to accurately control these systems have been detailed. Even with these criteria satisfied, the data at the lowest energy had poor statistical accuracy at higher scattering angles. It was, however, still possible to observe the trend in the changes to $L_\perp$ as the energy was lowered.

To provide a complete description of the scattering process it is important to also measure the atomic collision parameters $P_{\rm lin}$ and γ, which require the use of linearly polarized laser radiation. This work is in progress; however, the relative population of excited targets is considerably lower than found for the current measurements due to the linear optical pumping process that is employed, which leads to much higher spontaneous emission losses. A repumping laser beam is therefore essential for these studies, so that atoms in the $F = 0$ ground state can also participate in the laser excitation process. We are currently investigating a new method to add sidebands to the existing laser radiation, so as to satisfy these requirements. This method will use a new type of enhancement cavity that allows the intracavity doubling crystal to *simultaneously* produce radiation at the primary UV laser frequency, and at the correct sideband frequency. In this way the difficulty of sideband generation in the UV is transferred to the fundamental (visible) laser wavelength, where EOMs are efficient and easily available.

of the forward structures; however, little can be said about the data beyond $\theta_e = 90°$ due to the poor statistical accuracy of the data at this energy.

These results show that the orientation of the electron-excited $4d^{10}5p\ ^2P_{3/2}$ state changes rapidly with scattering angle, and that changes to the orientation are sensitive to changes in the energy of the interaction. For a fully coherent interaction it is possible to calculate the magnitude of the alignment parameter since in this case $P_{\rm lin} = \sqrt{1 - L_\perp^2}$; however, since the target is relatively heavy, this parameter should be determined independently.

No theoretical calculations of the ACPs for silver have yet been published, and so it is hoped that the results presented here over a wide range of energies will prompt further work in this area. Although silver is relatively heavy, it may not require a full relativistic treatment [31], and so nonrelativistic methods including convergent close coupling theories [32], distorted wave Born approximations [33], and R-matrix methods [34] should be reasonably accurate. These different methods have proven successful at predicting the ACPs for alkali and alkali-earth targets; however, it remains to be seen how accurate these different approaches will be for this more complex transition-metal target.

[1] N. Andersen, J. W. Gallagher, and I. V. Hertel, Phys. Rep. **165**, 1 (1988).

[2] I. V. Hertel and W. Stoll, J. Phys. B **7**, 570 (1974).

[3] I. V. Hertel and W. Stoll, Adv. At. Mol. Phys. **13**, 113 (1977).

[4] K. A. Stockman, V. Karaganov, I. Bray, and P. J. O. Teubner, J. Phys. B **31**, L867 (1998).

[5] D. S. Slaughter, V. Karaganov, M. J. Brunger, P. J. O. Teubner, and I. Bray, Phys. Rev. A **75**, 062717 (2007).

[6] P. W. Zetner, P. V. Johnson, Y. Li, G. Csanak, R. E. H. Clark, and J. Abdallah, J. Phys. B **34**, 1619 (2001).

[7] P. V. Johnson, B. Eves, P. W. Zetner, D. Fursa, and I. Bray, Phys. Rev. A **59**, 439 (1999).

[8] A. J. Murray and D. Cvejanovic, J. Phys. B **36**, 4889 (2003).

[9] B. V. Hall, Y. Shen, A. J. Murray, M. C. Standage, W. R. MacGillivray, and I. Bray, J. Phys. B **37**, 1113 (2004).

[10] M. Hussey, A. J. Murray, W. R. MacGillivray, and G. C. King, Phys. Rev. Lett. **99**, 133202 (2007).

[11] M. Hussey, A. J. Murray, W. R. MacGillivray, and G. C. King, J. Phys. B **41**, 055202 (2008).

[12] A. J. Murray, W. R. MacGillivray, and M. Hussey, Phys. Rev. A **77**, 013409 (2008).

[13] A. Knight-Percival, S. Jhumka, M. Hussey, and A. J. Murray, J. Phys. B **44**, 105203 (2011).

[14] M. Hussey, S. Jhumka, and A. J. Murray, Phys. Rev. A **86**, 042705 (2012).

[15] N. Andersen and K. Bartschat, Adv. At. Mol. Phys. **36**, 1 (1996).

[16] N. C. Blais and J. B. Mann, J. Chem. Phys. **33**, 100 (1960).

[17] Y. M. Smirnov, Tech. Phys. **44**, 137 (1999).

[18] S. D. Tošić, J. Phys.: Conf. Ser. **399**, 012004 (2012).

[19] S. D. Tošić, V. Pejcev, D. Šević, R. P. McEachran, A. D. Stauffer, and B. P. Marinkovic, Nucl. Instrum. Methods B **279**, 53 (2012).

[20] Frialit-Degussit ceramics, www.degussit.co.uk.

[21] EP4000 2×2000 W amplifier, Behringer amplifiers, www.behringer.com.

[22] Omega Industries: 5% W 5% Re:26% W 26% Re thermocouple wire, www.omega.co.uk.

[23] A. J. Murray, B. C. H. Turton, and F. H. Read, Rev. Sci. Instrum. **63**, 3346 (1991).

[24] J. N. H. Brunt, G. C. King, and F. H. Read, J. Phys. B **10**, 1289 (1977).

[25] K. L. Nixon and A. J. Murray, Phys. Rev. Lett. **106**, 123201 (2011).

[26] A. J. Murray, Meas. Sci. Technol. **23**, 107001 (2012).

[27] GLB10-UV BBO Glan-laser polarizer, Thorlabs, www.thorlabs.co.uk.

[28] QWPO-325-08-4-R10 zero-order $\lambda/4$ plate CVI, Melles Griot, www.cvimellesgriot.com.

[29] G. Uhlenberg, J. Dirscherl, and H. Walther, Phys. Rev. A **62**, 063404 (2000).

[30] P. M. Farrell, W. R. MacGillivray, and M. C. Standage, Phys. Rev. A **44**, 1828 (1991).

[31] R. K. Chauhan, R. Srivastava, and A. D. Stauffer, J. Phys. B **38**, 2385 (2005).

[32] D. V. Fursa and I. Bray, J. Phys. B **41**, 145206 (2008).

[33] R. T. Sang, P. M. Farrell, D. H. Madison, W. R. MacGillivray, and M. C. Standage, J. Phys. B **27**, 1187 (1994).

[34] O. Zatsarinny, K. Bartschat, L. Bandurina, and S. Gedeon, J. Phys. B **40**, 4023 (2007).